JOHANNES KEPLER
UNIVERSITY LINZ

SETUP TO MEASURE MAGNETIC FIELD EFFECTS ON THE PHOTOCURRENT IN ORGANIC SOLAR CELLS

Author
Lisa Berger

Submission
Institute of Physical Chemistry and Linz Institute for Organic Solar Cells

Thesis Supervisor
Assoc. Prof. Dr. Markus C. Scharber

September 2022

Bachelor's Thesis
to obtain the academic degree of

Bachelor of Science (BSc)
in the Bachelor's Program

Chemistry and Chemical Technology

JOHANNES KEPLER UNIVERSITY LINZ
Altenberger Straße 69
4040 Linz, Austria
jku.at

JOHANNES KEPLER
UNIVERSITY LINZ

SWORN DECLARATION

I hereby declare that the thesis submitted is my own unaided work, that I have not used other than the sources indicated, and that all direct and indirect sources are acknowledged as references.

Place, Date

Signature

Abstract

The outline of this work is to develop a measurement system at the Linz Institute of Organic Solar Cells (LIOS) to study the photocurrent of organic semiconductor-based photodiodes and solar cells in the presence of a magnetic field.

In order to overcome measurement issues and test operability of the resulting setup, the magnetic field effect on the photocurrent of several different fullerene and non-fullerene based organic bulk-heterojunction cells was investigated. The high-performance polymer D18 was the used donor material. The content of the non-fullerene (Y6) and the fullerene acceptor ($PC_{60}BM$) in the absorber layer was varied. The measurements in the magnetic field were done at various sample temperatures, different data recording protocols were applied and also the effect of the temperature in the laboratory was investigated. Additionally, the prepared devices were characterized with JV (current-volt), UV-VIS, photoluminescence (PL) and electroluminescence (EL) measurements.

Table of Contents

1. Introduction

Organic solar cells (OSCs) belong to the group of third generation cells. The active layer consists of carbon based π-conjugated molecules and polymers. They are especially interesting because they are industrially printable (roll-to-roll). This technique is low in energy consumption and makes the production cheaper compared to silicon solar cells [1]. The investigation of magnetic field effects on photocurrent (MFE) is a way to elucidate the recombination processes and charge carrier generation in bulk-heterojunction OSCs [2].

1.1. Materials

ITO coated glass was purchased at Xin Yan Technology LTD. The chemical structures of the used polymers and acceptor materials are shown in **Figure 1**. As hole transport material, PEDOT:PSS (Al4083) (a.) from Heraeus was used. The donor poly[(2,6-(4,8-bis (5-(2-ethylhexyl-3-fluoro)thiophen-2-yl)-benzo[1,2-b:4,5-b']dithiophene))-alt-5,5'-(5,8-bis(4-(2-butyloctyl)thiophen-2-yl)dithieno[3',2':3,4;2'',3'':5,6]benzo[1,2-c][1,2,5]thiadiazole)] (D18) (b.) and the acceptor 2,2'-((2Z,2'Z)-((12,13-bis(2-ethylhexyl)-3,9-diundecyl-12,13-dihydro-[1,2,5]thiadiazolo[3,4-e]thieno[2",3'':4',5']thieno[2',3':4,5]pyrrolo[3,2-g]thieno[2',3':4,5]thieno [3,2-b]indole-2,10-diyl)bis(methanylylidene))bis(5,6-difluoro-3-oxo-2,3-dihydro-1H-indene-2,1-diylidene))dimalononitrile (Y6) (c.) were purchased from 1-Material. [6,6]-Phenyl-C_{61}-butyric acid methyl ester ($PC_{60}BM$) (d.) was purchased from SolleneBV. Calcium and aluminum were used as electrode material.

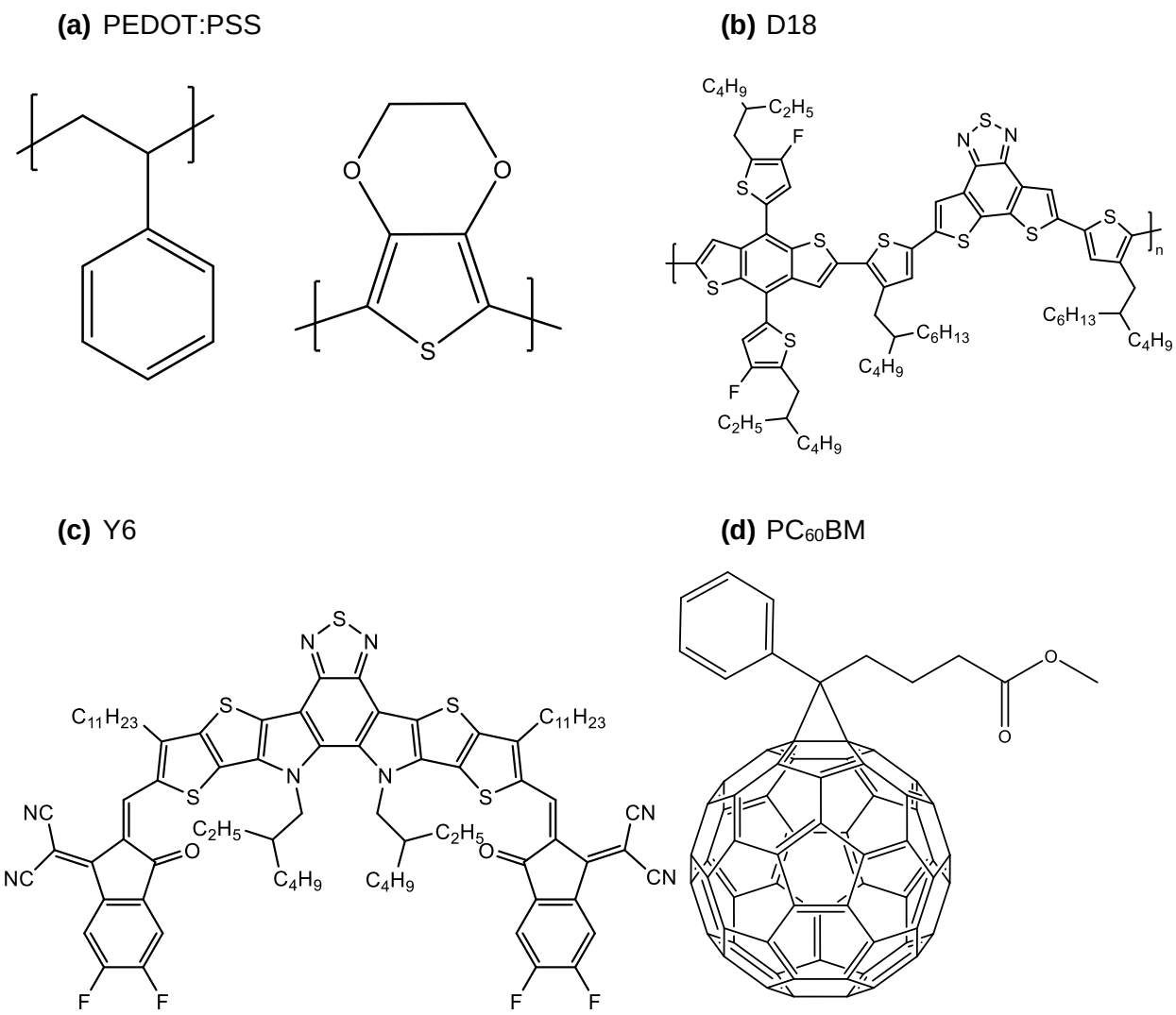

Figure 1. Chemical structures of the (a) hole transport layer PEDOT:PSS, (b) donor polymer D18, (c) non-fullerene acceptor material Y6 and (d) fullerene acceptor $PC_{60}BM$.

1.2. Theory

1.2.1. Organic solar cells (OSCs)

Organic solar cells consist of an organic semiconductor, cathode, anode and interfacial layers. The layers can be printed on foils or applied to glass substrates. Efficient charge generation happens in a donor-acceptor (D/A) blend. The used materials have different electron affinity and can be small molecules, polymers or a mixture of both. In the following, the necessary steps for utilizing solar radiation in a bulk heterojunction (BHJ) organic solar cell to generate electrical energy are described. Photoexcitation is required to generate current. The photoexcitation needs sufficient energy to promote one electron of from the HOMO (highest occupied molecular orbital) to the LUMO (lowest unoccupied molecular orbital) level in the donor. Such an absorbed photon creates a bound electron-hole pair, called exciton. The exciton has to diffuse to the donor-acceptor interface, where the electron is transferred to the energetically lower LUMO level of the acceptor. The now split charges drift/diffuse to the electrodes [3–5]. However, there are several recombination processes active in organic solar cells. In addition to radiative recombination, there are non-radiative recombination pathways, namely Auger recombination, surface recombination, and recombination via traps and intermediate states. The energy released by the recombination of two charge-carriers can be dissipated by the emission of a photon or several phonons. In the discussion within this thesis, recombination via molecular states is the most important pathway.

1.2.2. Organic semiconductors

This subchapter explains what charge carriers mean in organic molecules and where they originate from. An alternating sequence of single and double carbon-carbon bonds leads to a delocalization of π-bonds, called π-conjugated system. Large molecular structures consisting predominantly of a carbon-carbon backbone and hydrogens bound to them (hydrocarbons) with a conjugated π-system possess semiconducting properties [6]. In the form of polymers or macromolecules they are used as organic semiconducting materials. This group can be divided into donors and acceptors.

Neutral molecules are often arranged in an ordered ensemble, e.g. a crystal lattice. Adding a positive or negative charge to a molecule changes its geometry and distance to neighboring molecules, thereby distorting the crystal lattice. Free charge carriers with spin ½ together with the corresponding lattice are called polarons. A negative and a positive polaron are further on called electron e^- and hole h^+, respectively. A coulombically bound e^--h^+ pair is called exciton [7].

1.2.3. External magnetic field effects

This thesis deals with the changes of the photocurrent of an illuminated organic solar cell by an applied magnetic field, which is further on called magnetic field effect (MFE). It is given in percent and calculated as given in equation 1 [8].

$$MFE = \frac{S_B - S_0}{S_0} \times 100\% \qquad \text{eq. 1}$$

S_B and S_0 are the photocurrents with and without an applied magnetic field, respectively.
A positive MFE means that due to the influence of a magnetic field, the solar cell delivers a higher photocurrent. The negative MFE is the reduction of current with application of a magnetic field.
Photocurrent is the movement of free charge carriers. It is generated within an OSC either by exciton dissociation - forming polarons - or exciton-charge reaction [9]. Due to the short lifetime of singlet excitons in the range of 100 ps [7], it makes mechanisms with their involvement at room temperature negligible. For this reason, the focus is placed on polaron processes.
In general, the exact mechanisms for MFEs on the photocurrent are not fully elucidated. The most essential principles are explained below.

A singlet state describes a system, when two electrons (one in the π*-orbital, one in the π-orbital) are anti-parallel, giving a total spin of zero $\hbar$. In the triplet configuration, they align parallel giving a total spin of 1 $\hbar$. As the total spin state is given as the addition of the spins of all electrons in all orbitals, anti-parallel paired electrons contribute zero to the total spin. An external magnetic field cannot influence a system with zero total spin. For this reason, singlet states are not changed with an applied magnetic field [10].
The Jablonski diagram in **Figure 2** displays possible states of an electron and pathways of excitation and relaxation.

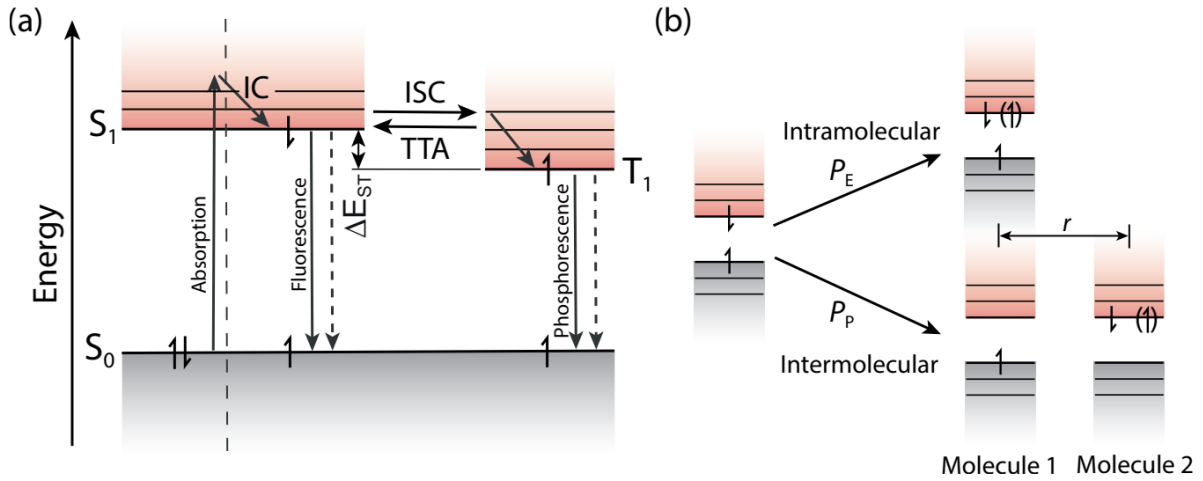

Figure 2. Jablonski diagram (a) different excitation, and relaxation pathways. Solid lines display radiative and dashed lines non-radiative processes. (b) intra- and intermolecular excited states [5].

S_0 denotes ground level and S_1 is the first singlet excited state. After photon absorption, an electron is excited to a higher energy regime. It can release energy as heat and rests at the lowest excited state afterwards. This process is called internal conversion (IC). Fluorescence describes the radiative emission of a photon from the excited singlet state, leading to energetic ground state. Due to IC, the emitted photons have lower energy than the absorbed ones, which is why a Stokes shift to higher wavelengths in fluorescence experiments can be observed. In an excited state, the electron can also change from singlet to triplet state or the other way around. Those mechanisms are called intersystem crossing (ISC) and triplet-triplet annihilation (TTA), respectively. Phosphorescence is the radiative recombination of a triplet state T_1 to the ground state S_0. Since the two involved states possess different spin symmetry, the conversion is spin-forbidden, hence slow [8]. ΔE_{ST} denotes the spin-exchange interaction energy. It is the energy difference occurring between the first excited singlet and triplet state [11]. As ΔE_{ST} decays with higher interradical distance, the recombination via the singlet-triplet pathway is facilitated [5].

There are several ways how an external magnetic field can change quantum processes within an OSC. Triplet state energy levels of polarons (spin = ½) undergo splitting in an external magnetic field, called Zeeman splitting. Thereby the energy difference between excited singlet and triplet states is changed [2].

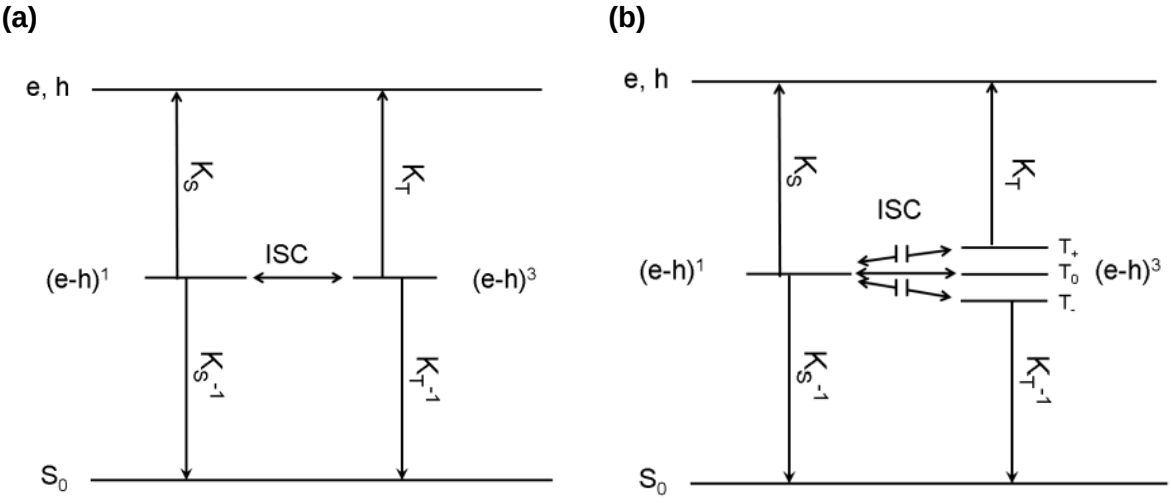

Figure 3. Energy diagrams of singlet and triplet polaron pairs in (a) zero magnetic field and (b) an external magnetic field [8].

In **Figure 3** (a), the singlet and the three triplet states are nearly in the same energy regime. The recombination of free charge carriers leads to a statistical population (1:3) of singlet pair (e-h)^1 and triplet states (e-h)^3. The electron-hole precursor pair (e-h)^1 or (e-h)^3 can dissociate, forming polarons e, h, or react and form an exciton [12]. An applied field causes splitting of the triplet state into three different energy levels, as can be seen in **Figure 3** (b). Due to splitting, just T_0 has an adequate energy level and ISC between singlet state and T_+ and T_- are suppressed. This causes a 1:1 singlet-triplet statistic. For this reason, intersystem crossing of singlet and triplet polaron pairs can be modified by an external magnetic field [2]. K_S and K_T denote the dissociation rate constants and K_S^{-1} and K_T^{-1} describe the recombination rate constant of singlet and triplet polaron pairs [8]. The alteration of the spin-mixing statistics in a magnetic field is a possibility to cause a MFE on the photocurrent [5]. In this case, recombination means the formation of excitons which can then relax to ground state. Since the external magnetic field leads to less mixing, there is less recombination, causing a positive MFE [12].

Another process is the triplet exciton - polaron mechanism. Triplet excitons can interact with polarons in terms of Coulombic scattering. Due to the longer triplet exciton lifetime compared to singlet excitons, their concentration can be large enough for interactions with polarons. Hence, those reactions may become significant. The scattering increases the diffusion pathway to the electrodes. Hence, the probability of recombination increases. The mobility of the free charges is decreased, and subsequently the photocurrent. A negative MFE can be detected [2,12].

2. Experimental

2.1. Fabrication of organic solar cells

The solar cells were built as bulk-heterojunction cells, meaning that the hole transport layer (HTL) is applied on top of the indium tin oxide (ITO) anode, followed by the photoactive layer (donor + acceptor) and cathode. PEDOT:PSS (Al4083) was used as HTL and calcium and aluminum were thermally evaporated as electrodes. The structure is depicted in **Figure 4**.

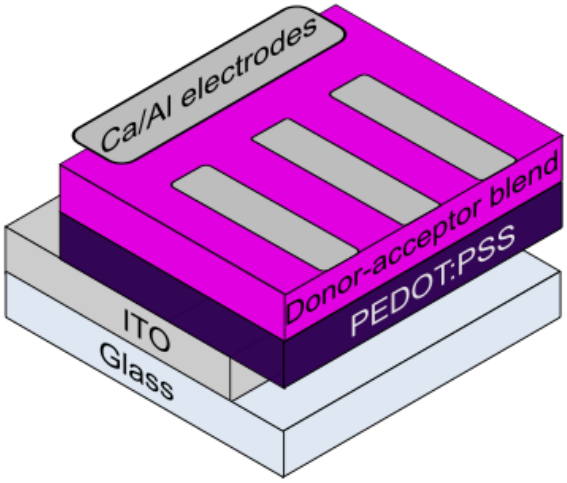

Figure 4. Structure of the fabricated organic solar cells.

From the ITO-coated glass substrates (1.5 × 1.5 cm) one third of the ITO film was etched with concentrated HCl to avoid the contact between anode and cathode later on. Cleaning was done with toluene, sonification in the 2 % cleaning agent “Hellmanex” in water (30 min at 80 °C), water and isopropanol (30 min at 40 °C), followed by oxygen plasma treatment (100 W, 5 min). PEDOT:PSS was filtered through a syringe filter (25 mm, 0.45 µm pore size, *VWR*) before spin-coating in atmospheric conditions. The layer was annealed at 150 °C for 10 minutes. The active layer comprising the polymer D18 blended with $PC_{60}BM$ or the non-fullerene acceptor Y6 was spin-coated in a water-free nitrogen atmosphere. As reference devices also photodiodes comprising pristine donor or acceptor materials were prepared. The total mass concentration of photoactive material in the processing solvent was 6 mg ml^{-1}. As top electrode, 10 nm calcium and 70 nm aluminum were thermally evaporated. As a last step, the cells were encapsulated using an epoxy resin purchased from *Emcast* and a glass slide.

In order to achieve different thicknesses of the active layer (in the range of 70 and 120 nm), the spin coating parameters were adjusted accordingly. The layer thickness was measured on a film coated glass substrate. The actual thickness of the active layer in the OSC can slightly deviate due to changed surface conditions caused by the additional PEDOT:PSS layer applied in full device stacks.

Two different batches of the D18 polymer were used. As the first used lot (lot#YY19088CB-1) was poorly soluble (≤2 mg ml^{-1}), it produced thin and inhomogeneous layers. A second lot (lot#YY17284CB) was applied with a mass concentration of 6.5 mg ml^{-1}. The addition of acceptor significantly improved the solubility. In order to ensure comparability, the mass concentration of all blend solutions used was 6.5 mg ml^{-1}. After experimenting with both, chloroform and chlorobenzene, chloroform was used as solvent for those cells undergoing further measurements. The active layer was applied at a solution temperature of 40 °C.

2.2. JV-curves

As first characterization method, the photoinduced current density was measured as a function of an applied voltage.
The radiance of the solar simulator was set to 100 mW/cm^2 AM1.5 by a reference silicon cell. A Keithely 2400 source-meter-unit and a custom-made labview software were used to record the current-voltage curves.

2.3. EQE

EQE stands for external quantum efficiency and depicts the efficiency of photon to extracted electron conversion of a solar cell.
The setup consists of a white lamp (*LOT ORIEL GRUPPE EUROPA*), chopper (*ORIEL Instruments*, mHz-kHz chopper controller), slit, monochromator, signal amplifier and a lock-in amplifier (SR830 DSP, *Stanford Research*). The modulated light beam illuminates the cell. The created photocurrent is amplified, and a voltage is recorded with the lock-in amplifier.

2.4. Electroluminescence (EL)

A Keithely 2400 was used to apply voltage at a fixed current to the solar cell. The emission of the devices was collected by a lens system and fed into an optical fiber. A monochromator (*Andor Shamrock 303i*) and a CCD-camera (*Andor IDUS 420A-OE*) were used to record the electroluminescence.

2.5. Photoluminescence (PL)

The photoluminescence of donor-acceptor blends on glass were measured. An OBIS 488 nm laser diode (*Coherent*) was used for photoexcitation. The emission of the devices was collected by a lens system and fed into an optical fiber. A monochromator (*Andor Shamrock 303i*) and a CCD-camera (*Andor IDUS 420-OE*) were used to record the electroluminescence. Long-pass filters in front of the monochromator were used to block the excitation light.

2.6. MFE – Photocurrent

The magnetic field effect was measured with the setup shown in **Figure 5**.

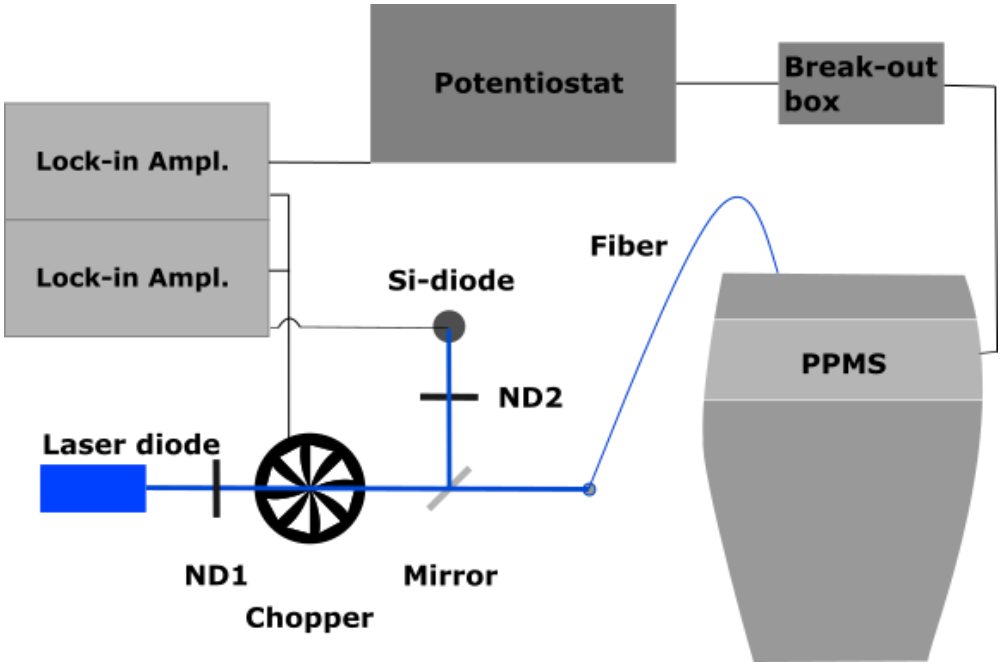

Figure 5. Schematic drawing of the setup of photocurrent detection of an OSC in the magnetic field.

The setup consists of an OBIS 488 nm laser diode from Coherent, a chopper-wheel and controller connected to two lock-in amplifiers (SR830 DSP, *Stanford Research*), a beam splitter, two neutral density filters (ND1 & ND2), a reference silicon diode (S2281, *Hamamatsu*), an optical fiber connected to the PPMS chamber, a break-out box, and a potentiostat (Modell 1002 T-NC, *Jaissle Potentiostat*).

The physical property measurement system (PPMS) from *Dynacool* (Quantum Design) is a cryostatic chamber which can be cooled with helium and its compression.

Figure 6 shows the design of the contacting site with a sample holder placed in it. Autodesk Fusion 360 was used to construct and design the 3D printed sample holder which was assembled as displayed in **Figure 7**. After printing the black polymer material, it was cleaned with 2-propanol and cured with UV light. The gold coated brass contacts were brazed onto the circuit board. A brass sheet is used to hold the OSC in place.

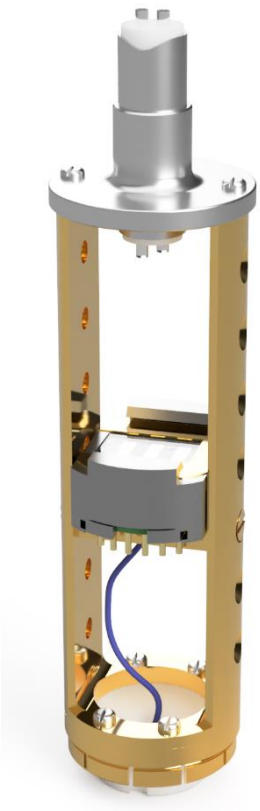

Figure 6. Solar cell placed in sample holder.

A pulsed laser beam is introduced into the PPMS chamber. In there is the 3D-printed sample holder equipped with the contacted solar cell.

The breakout box was necessary to get the connection of anode and cathode pins in the form of BNC cables. The generated photocurrent was amplified by the potentiostat which gave a proportional voltage as output. This is the function of a trans-impedance amplifier which was placed between the break-out box and the lock-in amplifier. After connection, the correct attachment of the measured pixel was checked by letting the dip switch on resting potential ("Ruhepotenzial"). Voltages below 2 V are displayed there. If the output is in an expected range, the dip switch is set to current ("I-Zelle"). Depending on the solar cell performance (current density), the current amplification was set between 0.1 and 10 µA (10^5 V/A to 10^7 V/A).

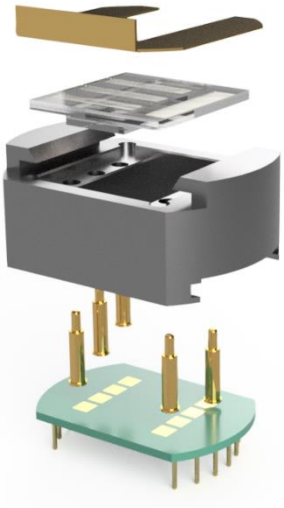

Figure 7. Assembly of the sample holder.

The settings on the lock-in amplifier were changed to improve the measuring output. In the following subchapter, different approaches are described. The MFE measurements in chapter 3.6. MFE were done with optimized settings.

Measuring with a lock-in amplifier requires a pulsed input signal. For this reason, a chopper was placed after the light source. The solar cell was illuminated with a frequency of 176 Hz giving a pulsed photocurrent output. A cord was connected from the chopper controller to the lock-in amplifier as an external reference source. A sine wave is then simulated at reference frequency. The device then multiplies the measurement signal with it. This way, a proportional DC signal originating just from inputs of the reference frequency is generated [13]. The reference silicon diode gave a current representing the laser intensity. The collected photocurrent data was corrected with the simultaneously measured laser power.

The measurements were conducted at different temperatures between 215 K and 295 K, whilst the field changed between ± 0.5 T. The magnetic field started at ± 0.5 T and had a data point at 0 T in the middle and at the end of the measurement. This way, the drift of the system could be estimated and - to a certain extent - the validity of the collected data approved.

3. Results and Discussion

3.1. Optimization setup MFE

The duration of the experiment showed an impact on the measurement results. There are two influencing parameters: laser drift and fluctuation of the magnetic field. Next to the sample, a reference Si-diode was illuminated simultaneously with the same laser beam via a beam splitter. Then the resulting current was referenced with the transformed PPMS photocurrent signal.

The calculations were done as follows:

First, the laser current signal was normalized, giving a signal of 1 at the highest intensity. Then the voltage output of the transformed photocurrent measurement of the solar cell was divided by the corresponding normalized laser signal. Lastly, equation 1 was applied, giving the MFE on photocurrent in percent.

$$MFE = \frac{S_B - S_0}{S_0} \times 100\%$$

As the drifts are supposed to be held as small as possible but a higher number of measuring points means smoother measurement curves, 72 data points were measured for each composition. An averaging of 3 per magnetic field measurement and data point were done.

Many of the curves showed severe asymmetry. The diagrams depicted in chapter 3.6. MFE are already the optimized results. Air conditioning and the resulting temperature difference for the laser could cause some drift. However, a test without air conditioning showed no significant improvement. It could still influence the laser stability since the stabilization of the temperature might be time delayed. The main factor of apparent time-dependent signal drifts was temperature difference. In general, the reduction of temperature decreased the photocurrent more pronounced than the external magnetic field. Since the MFE is given in percent, this influence is not apparent in the given diagrams. Between each measuring temperature there was a minimum waiting time of 40 minutes. The detected difference between the two temperature sensors in the PPMS had to be below 2.5 K. Otherwise, during the duration of the measurement, the changing temperature would cause asymmetry. This rather pronounced effect is shown in **Figure 8**. The measurement was done when the chamber was not stabilized and not cooled down enough. As the photocurrent decreases with decreasing temperatures, the magnetic field effect just appears to be larger in the higher temperature regime compared to the stabilized temperature data point. Considering equation 1, this is caused by the applied mathematical method. Assuming the temperature difference between both sensors to be around 2.5 K and the used measurement settings, it takes 15 to 20 minutes to reach the data point without magnetic field S_0. Due to the time delay, S_0 is measured at the desired temperature. Therefore, the reference signal S_0 is smaller than it would have been those 15 to 20 minutes before at descending temperature.

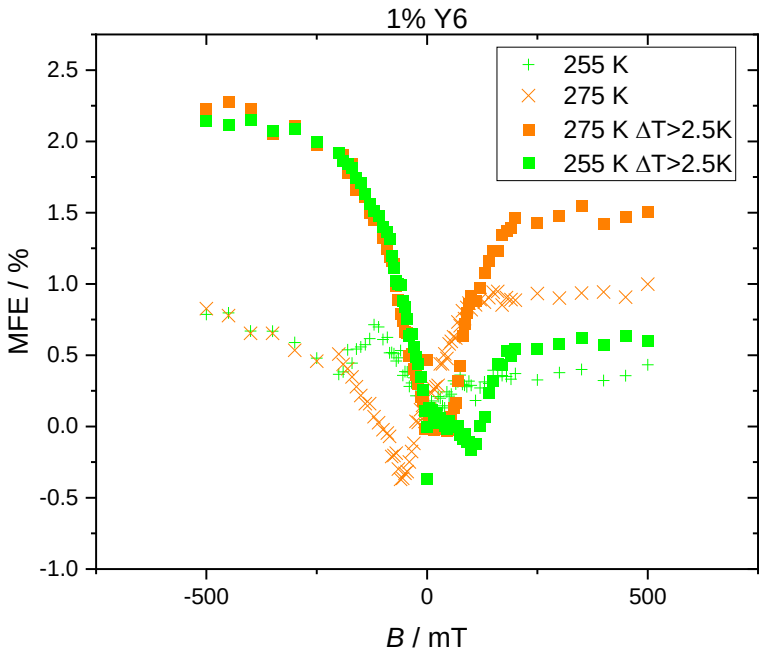

Figure 8. Effect of temperature drift on MFE.

A further optimization strategy was the suppression of vibrations. As the connector box was stored on an elevated wooden place, a decoupling of resonances was done with various isolating materials. Furthermore, the cables and connectors were kept on their designated spot without movement.

Parts of the setup were tested for drift stability. Furthermore, it should be ensured that there is no tilting of the sample holder within the magnetic field. For this purpose, an empty glass substrate was put into the sample holder of the PPMS. The fluorescence change was measured. This method was intended to show the laser and magnetic field stability. However, since the fluorescence and not the photocurrent was measured, there is another detector system which might lead to different aberration. The result is shown in **Figure 9**.
The drift variation appears to be in the range of ± 0.2 % in MFE_{PL}. However, before improving the connector stability (fixed, without movement, with reduced vibration), the deviations were up to 1 % MFE.

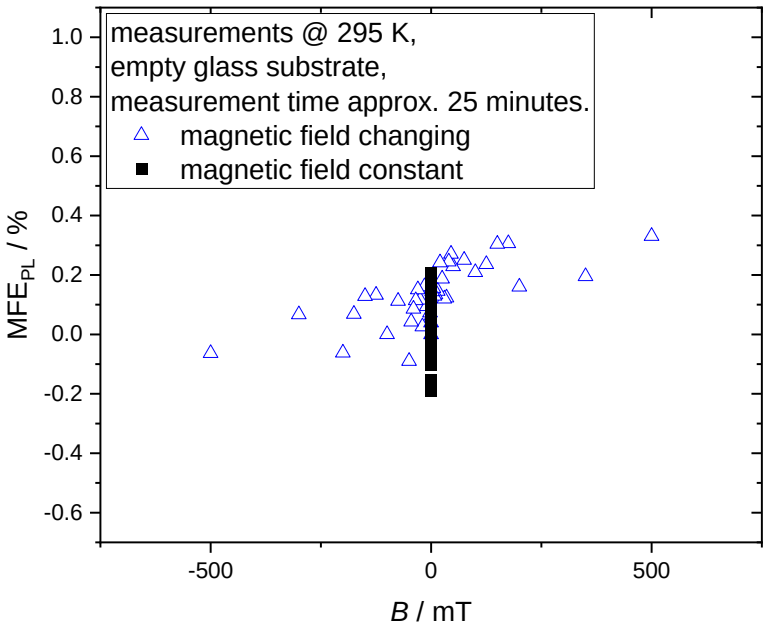

Figure 9. Drift stability of the setup disregarding photocurrent detection.

The data measurements were usually done by using a gradually in-/ or decreasing magnetic field. In **Figure 10**, the data points were collected in a disordered manner meaning that the magnetic field changed from a positive to a negative to a positive magnetic field value.

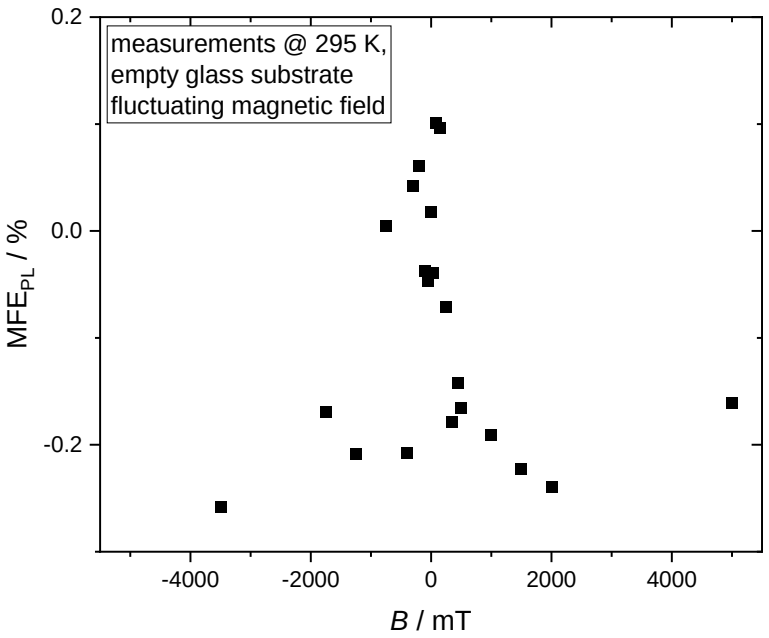

Figure 10. Accuracy and reproducibility of the MFE setup and results of non-progressively measured data points with respect to the magnetic field.

Compared to the measurements in the gradually changing magnetic field in **Figure 9**, the non-progressively collected data points appear to peak at zero-field conditions in **Figure 10**. However, the general deviation in photoluminescence is in the same range of ± 0.2 % in MFE_{PL}. This resembles the fluctuation without an applied field.

3.2. JV-curves

Table 1 summarizes the JV-characteristics of the fabricated OSCs with changing active layer composition. The percentage of acceptor material is given with respect to D18. V_{OC} is the open-circuit potential, I_{SC} is the short-circuit current, *FF* is the fill-factor, *PCE* is short for power conversion efficiency, P_{light} is the power of the solar simulator. Those factors relate according to equation 2.

$$PCE = \frac{V_{OC} \cdot I_{SC} \cdot FF}{P_{light}} \qquad \text{eq. 2}$$

The fabricated solar cells show rather low efficiencies (**Table 1**). However, the non-ideal donor-acceptor ratios were chosen on purpose, intending to achieve larger MFEs. Within more ideal conditions D18:Y6 with a D/A ratio of 1:1.6 yielded PCEs of 14-16 % [14].

Table 1. JV-characteristics of D18 cells with respective acceptor share. The values in brackets refer to the respective cell used for measurements in the magnetic field. J_{SC} is the current density, *n* describes the total number of devices used to determine the average device parameters.

Active layer	V_{OC} **/ V**	J_{SC} **/ mA cm^{-2}**	***FF* / %**	***PCE* / %**	***n***
50% Y6	0.75 (0.73)	10.58 (10.51)	0.60 (0.53)	4.75 (4.06)	4
10% Y6	0.65 (0.64)	1.70 (1.95)	0.27 (0.27)	0.30 (0.33)	5
5% Y6	0.64 (0.67)	0.42 (0.43)	0.24 (0.25)	0.07 (0.07)	8
1% Y6	0.62 (0.68)	0.16 (1.82)	0.31 (0.28)	0.03 (0.34)	5
pure D18	1.12 (1.23)	0.032 (0.031)	0.37 (0.37)	0.01 (0.01)	5
50% PCBM	0.90 (0.94)	3.69 (3.87)	0.51 (0.54)	1.71 (1.98)	5
10% PCBM	0.83 (0.80)	1.33 (1.00)	0.27 (0.26)	0.29 (0.21)	6
5% PCBM	0.81 (0.86)	0.36 (0.45)	0.26 (0.26)	0.08 (0.10)	5
1% PCBM	0.80 (0.75)	0.23 (0.21)	0.32 (0.33)	0.06 (0.05)	4

Both acceptor series of JV-curves (Appendix) show the increase of current density with increasing acceptor ratio. The JV-curves of both 50% acceptor cells show the dark curve as the shifted curve under radiation.

The JV-curve of the 50% PCBM cell shows the desired rapid incline starting at 0.91 V and is nearly just the y-shifted dark curve.

A reason for the deviation of an ideal solar cell system is the limited mobility of electrons in the predominately hole transporting donor material. This is the case since the donor/acceptor ratios are below the percolation limit [15].

3.3. UV-VIS

The absorption spectra were measured on thin films on glass. The spectra of the pristine donor and acceptor materials are depicted in **Figure 11**. $PC_{60}BM$ has a peak at 337 nm. Its spectrum is in accordance with literature [16]. The absorption peaks of D18 appear at 543 nm and 578 nm, whilst Y6 absorbs most at 829 nm. The spectrum is in accordance with literature as well [14].

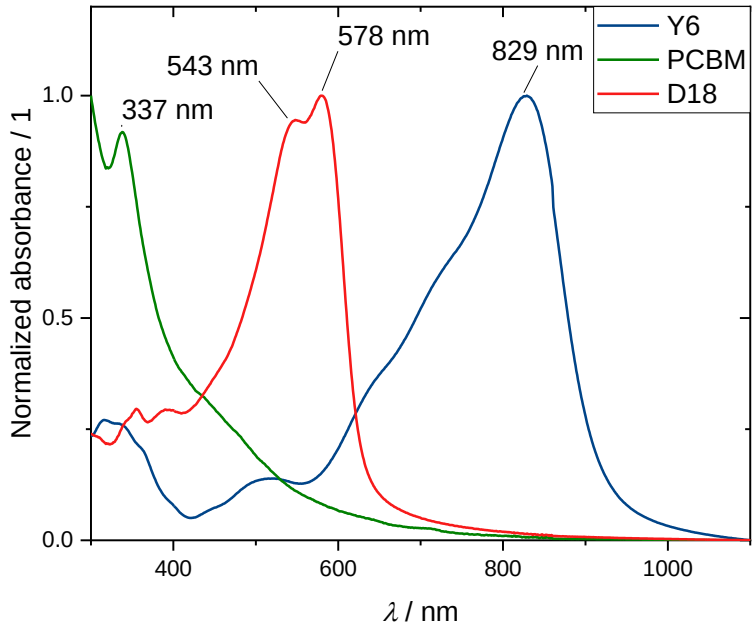

Figure 11. UV-VIS absorption spectra of pristine Y6, $PC_{60}BM$, and D18.

Figure 12 shows the influence of changing donor-acceptor mixtures on the absorption. The spin-coated films had a thickness of 40-60 nm. Both diagrams, (a) and (b) show distinct peaks for the donor and acceptor material. The graphs normalized with the glass absorption peak fit to the mixture ratios.

(a) **(b)**

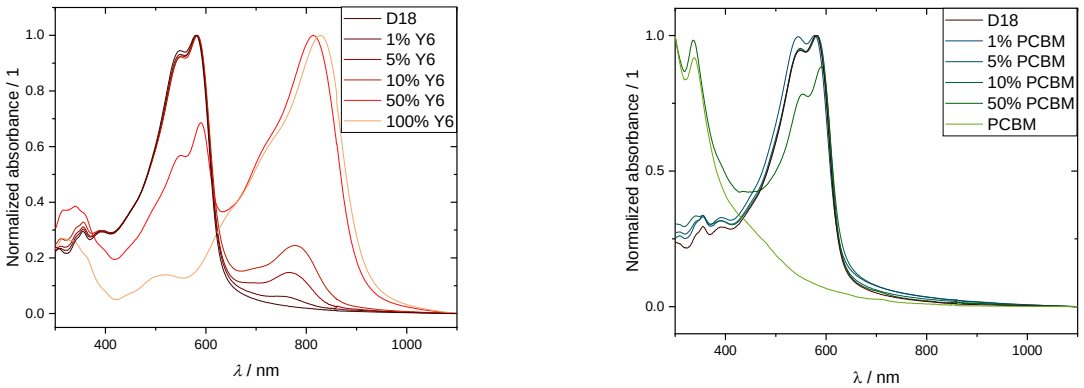

Figure 12. Normalized absorption spectra of D18 blends with changing acceptor concentration, namely (a) Y6 and (b) $PC_{60}BM$.

3.4. Fluorescence

For the photoluminescence experiments, the same samples were used as for the UV-VIS measurements. **Figure 13** (a) shows normalized photoluminescence spectra of D18 blends with increasing Y6 concentration. A shift to higher wavelengths, thus into the lower energy regime, was detected. In **Figure 13** (b) the photoluminescence spectra of D18 blends with increasing $PC_{60}BM$ concentration are plotted.

(a) **(b)**

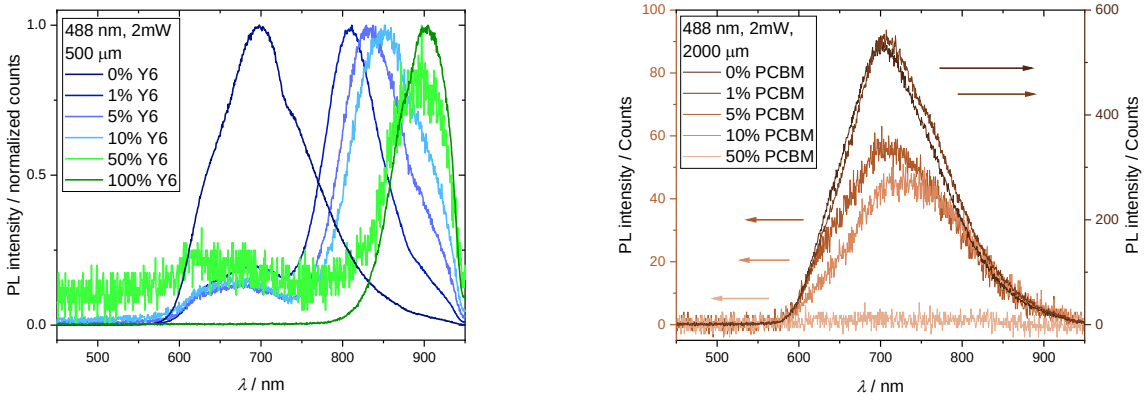

Figure 13. Results of photoluminescence experiments of (a) D18:Y6 blend films displayed with normalized counts, and (b) D18:$PC_{60}BM$ blend films in absolute counts.

Table 2 shows the PL quenching of the donor peak with addition of acceptor, which is observed for $PC_{60}BM$ and Y6. However, these values cannot be taken as completely accurate, since the changed acceptor ratios lead to different layer thicknesses and absorption. Compared to the UV-VIS measurements, there is a pronounced stokes shift of the PL data. This shows the energy loss from absorption to emission [17].

Table 2. Photoluminescence quenching factors of blends with different acceptor ratios in D18 (rounded) compared to pristine D18.

	1 %	5 %	10 %	50 %
Y6	5	75	125	1000
$PC_{60}BM$	0	9	11	> 130

Larger and pure donor and acceptor domains within the photoactive layer are a possible reason for exiguous PL quenching [15]. An addition of Y6 led to a shift of the D18 photoluminescence peak at 698 nm to 904 nm. Increasing the acceptor concentration up to 50 % led to quenching of the signal. Therefore, the improvement of exciton harvest with increasing acceptor ratio is assumed. The peak of the non-normalized pure Y6 film is larger than of the 1:1 D/A blend. It could indicate less efficient exciton harvest in the active layer consisting of just acceptor [15]. The shift of absorption of Y6 in different solvents and blends was explained by changes in aggregation. In literature, the absorption at higher wavelength means lower level of aggregation [18]. In this work, these shifts did not appear in UV-VIS measurements but PL.

Figure 14 displays the electroluminescence peaks and the photoluminescence measurements for each blend ratio. In general, blue shifted peaks are higher in energy, red shifted ones are lower in energy. This means that the electric excitation led to higher energy photons compared to laser excitation with a wavelength of 488 nm for all cells, except the 10 % PCBM cell.

Comparing both different acceptor systems, the Y6 cells show higher fluorescence in PL and EL measurements. Increasing the Y6 content shifts all peaks to higher wavelengths. Whilst the PL measurements show two peaks, EL measurements gave one approximately 10 nm blue-shifted peak. For example, in the 1 % Y6 cells peaks are at 680 nm and 810 nm for PL, and at 800 nm for EL, respectively.

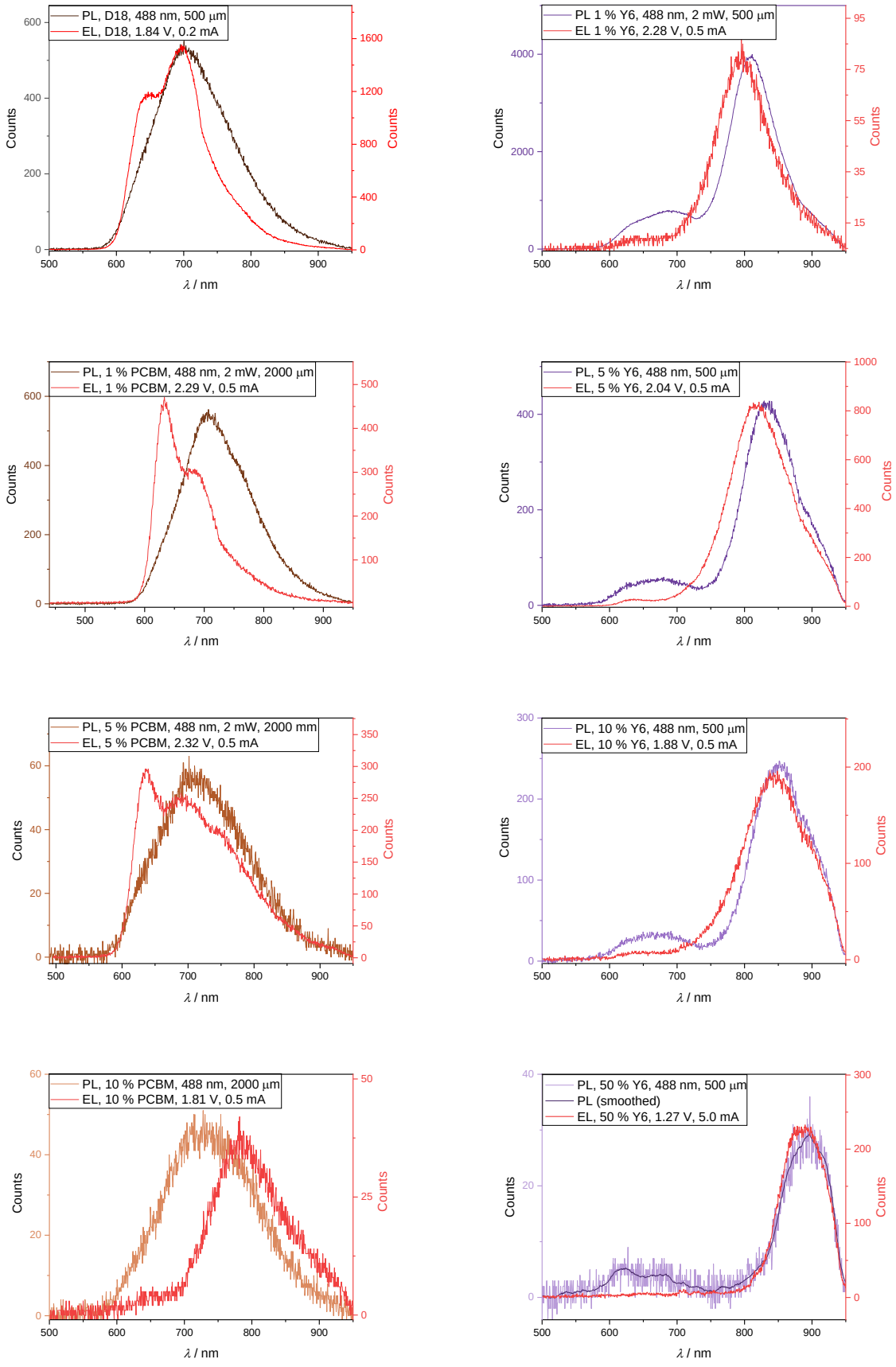

Figure 14. Photoluminescence and electroluminescence measurements of solar cells. The active layer consists of pure D18 (a), and blends of D18 mixed with: 1 % PCBM (b), 5 % PCBM (c), 10 % PCBM (d), 1 % Y6 (e)%, 5 % Y6 (f), 10 % Y6 (g), and 50 % Y6 (h).

3.5. External quantum efficiency (EQE)

EQE is the external quantum efficiency. It describes the ratio of photons converted into extracted electrons by the solar cell. The calculations for the diagrams were done as follows:

$$EQE = \frac{R_{SC} \cdot S_{Si} \cdot h \cdot c}{R_{Si} \cdot \lambda \cdot e} \times 100\% \qquad \text{eq. 3}$$

with $R=(x^2+y^2)^{0.5}$ as the measured signal in mV for the solar cell and silicon reference with the subscripts SC and Si, respectively. S_{Si} is the value of the sensitivity curve for the reference diode in A W^{-1}. The wavelength λ was inserted in m, h is the Boltzmann constant in J s, c is speed of light in m s^{-1}, and e is the elementary charge in C.

In **Figure 15** and **Figure 16**, the EQE spectra are displayed together with the absorption spectrum of the corresponding solar cell.
The absorption edge of the D18 EQE curve fits to the absorption measurement. Due to addition of Y6, a second absorption peak arises at 780 nm. With increasing acceptor content, the EQE rises in general. Additionally, the height of both peaks assimilates in the solar cell with the 1:1 (w/w) D/A-ratio in the active layer. The signal shape with its maxima at 590 nm and 780 nm is in correspondence with the UV-VIS measurement.
The 0 %, 1 %, 5 %, 10 % and 50 % Y6 acceptor ratio yield an EQE of 1.3 %, 1.4 %, 5.4 %, 10.0 %, 39.5 % at 590 nm, and 0 %, 0.1%, 1.8 %, 4.3 % and 38.0 % in the range between 770 and 820 nm, respectively.

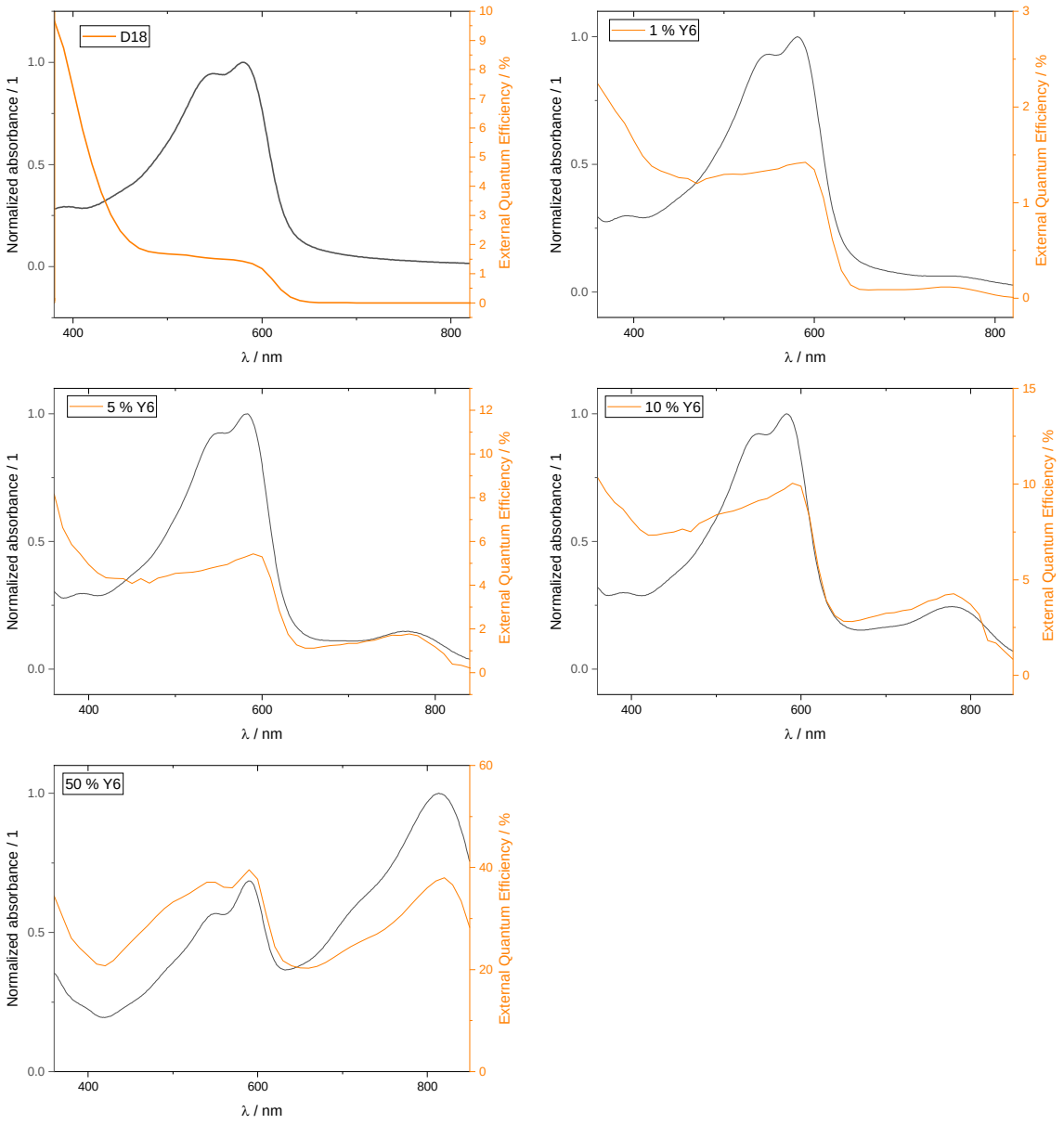

Figure 15. EQE and absorption spectra of the OSCs consisting of the donor D18 with rising Y6 acceptor content.

Figure 16 displays the absorption spectra of D18:$PC_{60}BM$ blends on glass substrates and the measured EQE of manufactured OSCs. The EQE at 590 nm is enhancing with rising acceptor concentration. It results in 1.3 %, 1.4 %, 1.4 %, 7.4 % and 29.3 % from 0 to 50 % $PC_{60}BM$ concentration. A more pronounced efficiency leap occurs between 5 % and 10 % acceptor concentration. Compared to Y6, this effect is more pronounced for $PC_{60}BM$ cells. This phenomenon can be explained by the percolation limit. The percolation threshold is defined as the lower limit of mixture ratio of materials which allow electron transport [19]. Above the binodal composition, there are two phases (donor and acceptor), below there is one mixture. The phase aggregation close to the percolation threshold is necessary to

provide sufficient electron percolating pathways [19]. However, aggregation is temperature dependent. A disadvantageous composition and resulting altered morphology can reduce the interfacial area for charge generation [15].

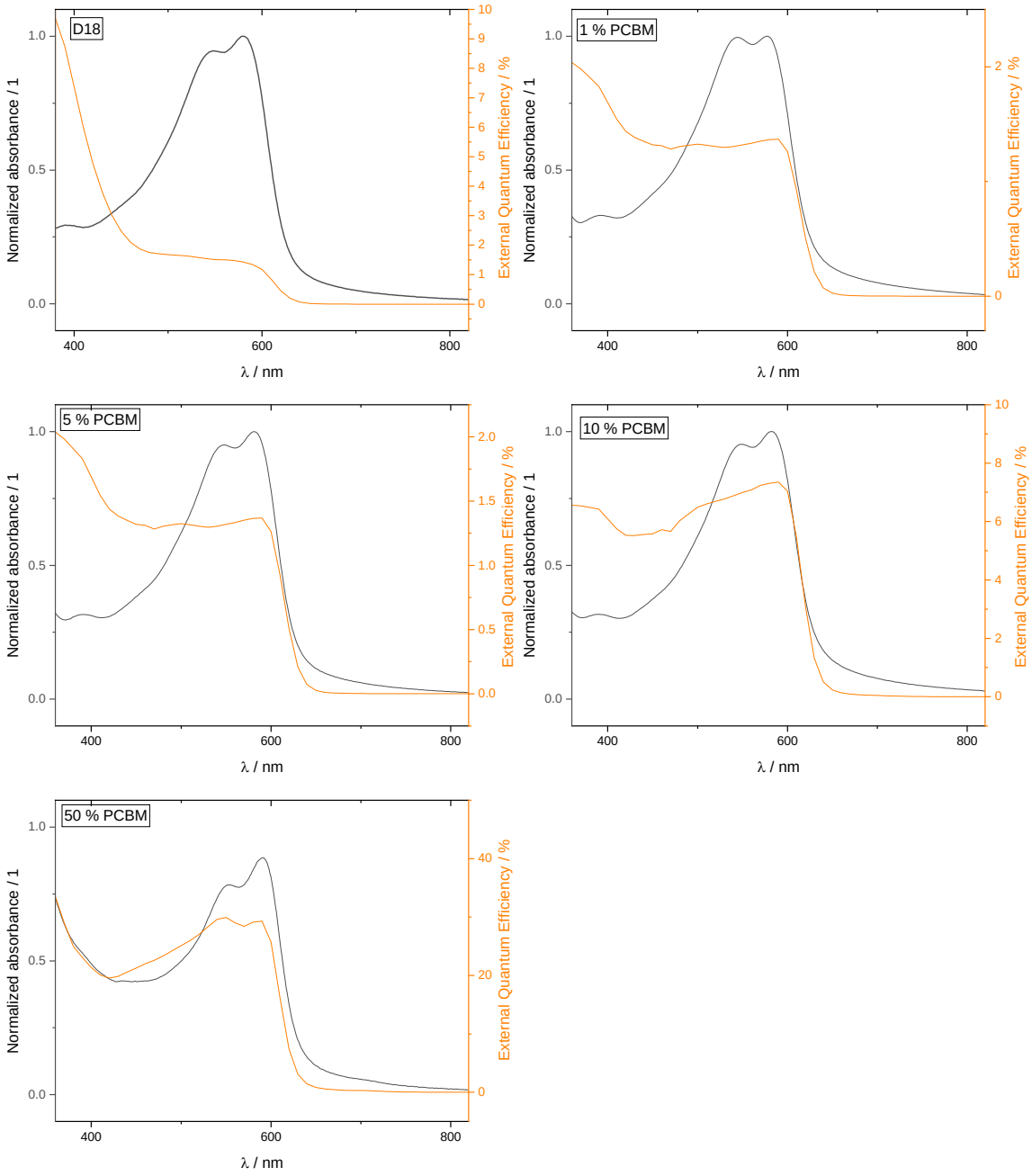

Figure 16. EQE and absorption spectra of the OSCs consisting of the donor D18 with rising $PC_{60}BM$ acceptor content.

3.6. MFE

Figure 17 and **Figure 18** show the measured MFE data using the optimized setup described in chapter 3.1. Optimization setup.

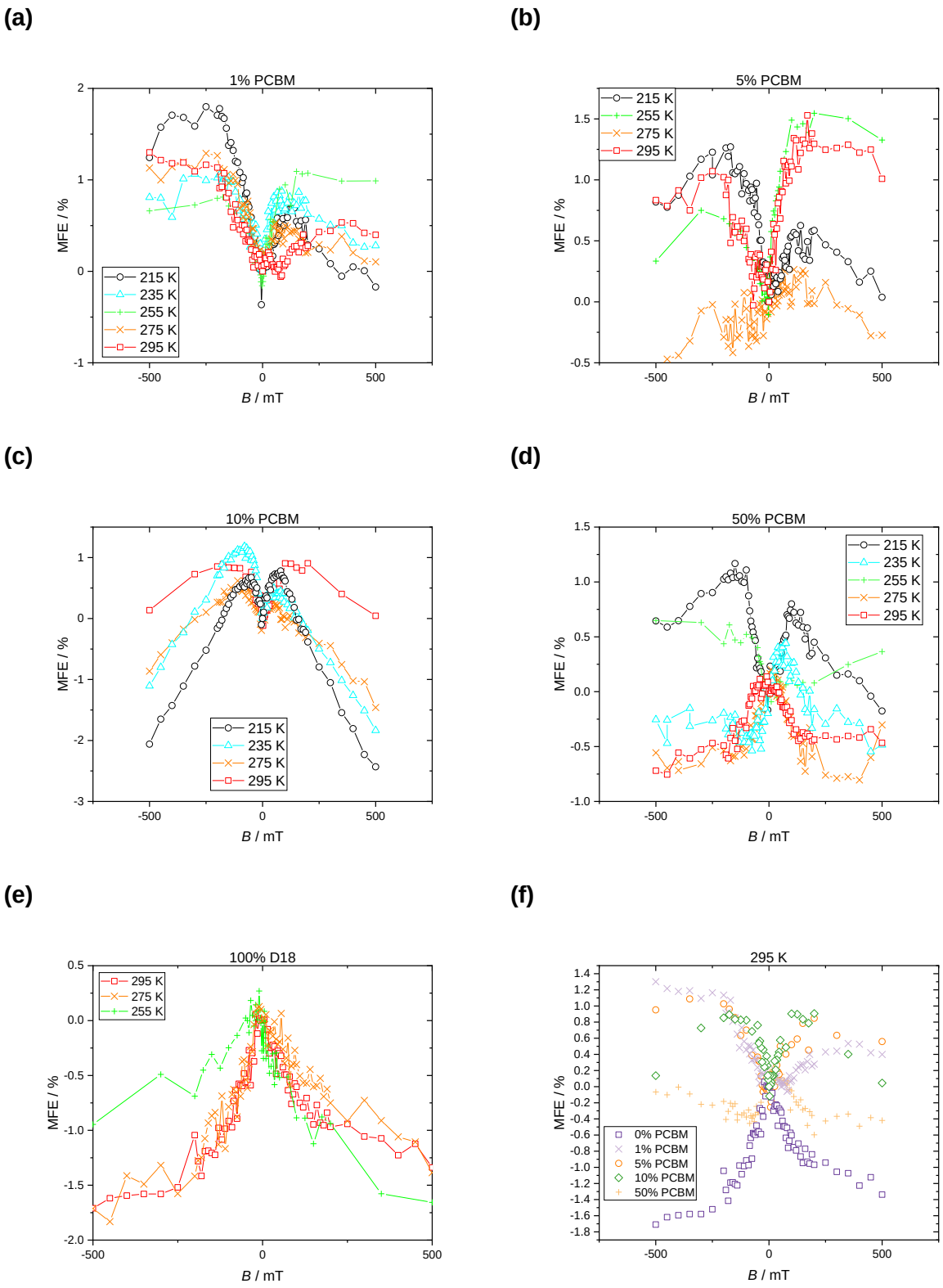

Figure 17. MFE in D18:$PC_{60}BM$ OSCs with (a) 1% $PC_{60}BM$, (b) 5 % $PC_{60}BM$, (c) 10 % $PC_{60}BM$, (d) 50 % $PC_{60}BM$, and (e) 0 % $PC_{60}BM$ content. A comparison of the measured data at 295 K is shown in (f).

Most $PC_{60}BM$ cells show a positive MFE up to 200 mT. Then the effect becomes negative. However, there is a negative MFE detectable for the 50 % $PC_{60}BM$ cell at 235, 275 and 295 K.

The D18 cell shows a negative MFE at given temperatures. When further cooled down to 235 K, there was an indistinct signal detectable.

The first positive, followed by a negative MFE indicates the involvement of the triplet exciton - polaron mechanism [12].

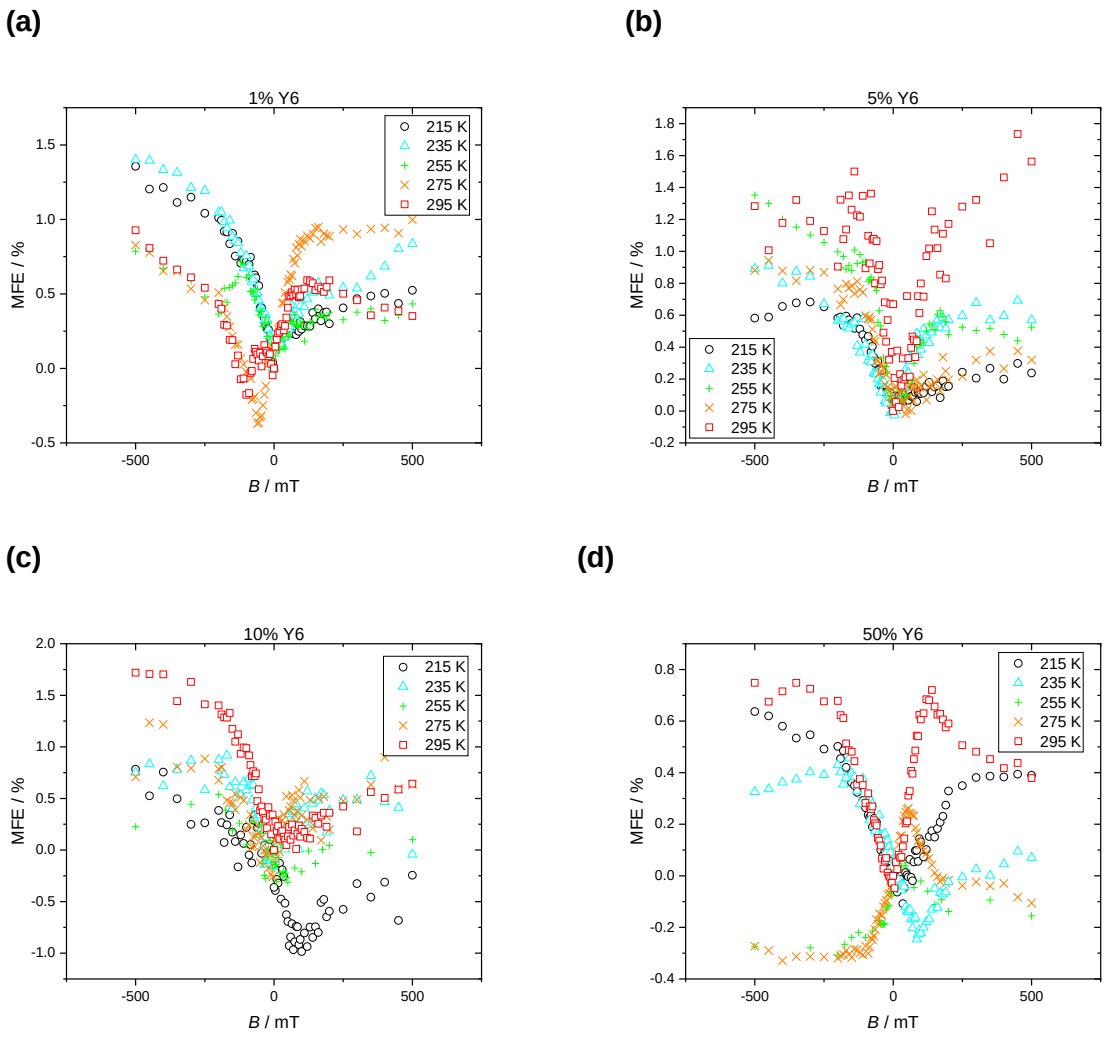

Figure 18. MFE in D18:Y16 OSCs with (a) 1 % Y6, (b) 5 % Y6, (c) 10 % Y6, (d) 50 % Y6.

The Y6 cells show mainly positive magnetic field effects. Within the measured range there is no level crossing visible in the form of a first positive and then negative MFE. The only negative curve is the 50 % Y6 cell at 275 K.

According to the explanation in chapter 1.2.3. External magnetic field effects, these positive MFE graphs indicate the suppression of spin-mixing as main pathway.

The changes with temperatures could be connected to mobility changes, however there is no distinct temperature trend in the collected data.

4. Summary & Conclusion

The overall goal of this thesis was to set up an experiment using a physical property measurement system to determine the magnetic field effect on the photocurrent of organic solar cells. The experimental results discussed above proof that this goal has been achieved. While optimizing the measurements procedure, several important experimental parameters could be identified. For a stable excitation intensity at the sample a constant temperature in the laboratory, no change in air flow, no extraneous light and an excellent laser alignment are very important. For the measurement itself, a constant sample temperature in the PPMS chamber and excellent electrical connections are essential. Since the mobility of charge carriers in organic semiconductors and most of the organic solar cell device parameters are temperature dependent, the sample temperature is so important. With the optimization of the experimental conditions, temperature drifts during the experiment could be reduced and more symmetric magnetic field effects were observed. Another important finding was that electrical measurements could only be performed when using a potentiostat as trans-impedance amplifier for photocurrent produced by the solar cell. Feeding the photocurrent directly into the lock-in amplifier led to random signal overload events in the lock-in.

In case of UV-VIS measurements, the experimental results are in line with results published in scientific literature. Solar cells with different active layer compositions were prepared and characterized. The presented results illustrate the importance of the donor-acceptor ratio in these devices. For small donor concentration, power-conversion efficiencies and external quantum efficiencies were rather low.

Comparing the fullerene and non-fullerene systems, PL quenching was more pronounced for the Y6 system. Concerning the magnetic field effects on photocurrent for the fullerene and non-fullerene OSCs, a distinct difference was observed. The majority of D18:$PC_{60}BM$ solar cell measurements showed a positive MFE at low magnetic fields and then negative MFE at higher fields. A merely positive MFE was detected for the majority of D18:Y6 solar cells. Interestingly, the pristine donor D18 gave a negative MFE. Although the recombination pathways are not fully elucidated, it is possible to differentiate between basic principles like changing the recombination statistics for electron and hole and the triplet exciton - polaron mechanism.

Concluding, the optimized setup can now be used for magnetic field measurements. An improvement of the sample holder allowing an easier and more reliable mounting of the samples might be possible. It would be quite interesting to compare the influence of the magnetic field on photocurrent to its influence on photoluminescence. As the radiative recombination would be detected as well, the charge carrier evolution and recombination processes could be better understood.

5. References

[1] Shaheen, S. E.; Ginley, D. S.; Jabbour, G. E. Organic-Based Photovoltaics: Toward Low-Cost Power Generation. *MRS Bull.* **2005**, *30*, 10–19. DOI: 10.1557/mrs2005.2.

[2] Xu, Z. Magnetic Field Effects on Photocurrent and Photovoltaic Processes in Organic Solar Cells, *Dissertation*, University of Tennessee, USA, **2008**.

[3] Brédas, J.-L.; Beljonne, D.; Coropceanu, V.; Cornil, J. Charge-transfer and energy-transfer processes in pi-conjugated oligomers and polymers: a molecular picture. *Chemical reviews* **2004**, *104*, 4971–5004. DOI: 10.1021/cr040084k.

[4] Nickel, F. *Herstellung und Charakterisierung mechanisch flexibler organischer Solarzellen durch Flüssigprozessierung*; KIT Scientific Publishing, Karlsruhe, **2014**.

[5] Putz, C. Flexible organic solar cells based on non-fullerene acceptors, *Master thesis*, Johannes Kepler Universität, Austria, **2020**.

[6] Choy, W. C. *Organic Solar Cells: Materials and Device Physics,* Springer, London, **2013**.

[7] Köhler, A. *Electronic processes in organic semiconductors: An introduction*, Wiley-VCH Verlag GmbH & Co: Weinheim, **2015**.

[8] Hu, B.; Yan, L.; Shao, M. Magnetic-Field Effects in Organic Semiconducting Materials and Devices. *Adv. Mater.* **2009**, *21*, 1500–1516. DOI: 10.1002/adma.200802386.

[9] Xu, Z.; Hu, B. Photovoltaic Processes of Singlet and Triplet Excited States in Organic Solar Cells. *Adv. Funct. Mater.* **2008**, *18*, 2611–2617. DOI: 10.1002/adfm.200800331.

[10] Köhler, A.; Bässler, H. Triplet states in organic semiconductors. *Materials Science and Engineering: R: Reports* **2009**, *66*, 71–109. DOI: 10.1016/j.mser.2009.09.001.

[11] Köhler, A.; Beljonne, D. The Singlet–Triplet Exchange Energy in Conjugated Polymers. *Adv. Funct. Mater.* **2004**, *14*, 11–18. DOI: 10.1002/adfm.200305032.

[12] Janssen, P.; Cox, M.; Wouters, S. H. W.; Kemerink, M.; Wienk, M. M.; Koopmans, B. Tuning organic magnetoresistance in polymer-fullerene blends by controlling spin reaction pathways. *Nature communications* **2013**, *4*, 2286. DOI: 10.1038/ncomms3286.

[13] Stanford Research Systems. User Manual: MODEL SR830 DSP Lock-In Amplifier, **2011**.

[14] Hofinger, J.; Putz, C.; Mayr, F.; Gugujonovic, K.; Wielend, D.; Scharber, M. C. Understanding the low voltage losses in high-performance non-fullerene acceptor-based organic solar cells. *Mater. Adv.* **2021**, *2*, 4291–4302. DOI: 10.1039/D1MA00293G.

[15] Wang, Z.; Peng, Z.; Xiao, Z.; Seyitliyev, D.; Gundogdu, K.; Ding, L.; Ade, H. Thermodynamic Properties and Molecular Packing Explain Performance and Processing Procedures of Three D18:NFA Organic Solar Cells. *Adv. Mater.* **2020**, *32*, 2005386. DOI: 10.1002/adma.202005386.

[16] Distler, A.; Sauermann, T.; Egelhaaf, H.-J.; Rodman, S.; Waller, D.; Cheon, K.-S.; Lee, M.; Guldi, D. M. The Effect of PCBM Dimerization on the Performance of Bulk Heterojunction Solar Cells. *Adv. Energy Mater.* **2014**, *4*, 1300693. DOI: 10.1002/aenm.201300693.

[17] Zou, X.; Wen, G.; Hu, R.; Dong, G.; Zhang, C.; Zhang, W.; Huang, H.; Dang, W. An Insight into the Excitation States of Small Molecular Semiconductor Y6. *Molecules* **2020**, *25,* 4118*.* DOI: 10.3390/molecules25184118.

[18] Wang, Y.; Zhuang, C.; Fang, Y.; Kim, H. D.; Yu, H.; Wang, B.; Ohkita, H. Improvement of Exciton Collection and Light-Harvesting Range in Ternary Blend Polymer Solar Cells Based on Two Non-Fullerene Acceptors. *Nanomaterials* **2020**, *10.* DOI: 10.3390/nano10020241.

[19] Ye, L.; Li, S.; Liu, X.; Zhang, S.; Ghasemi, M.; Xiong, Y.; Hou, J.; Ade, H. Quenching to the Percolation Threshold in Organic Solar Cells. *Joule* **2019**, *3*, 443–458. DOI: 10.1016/j.joule.2018.11.006.

APPENDIX

(a)

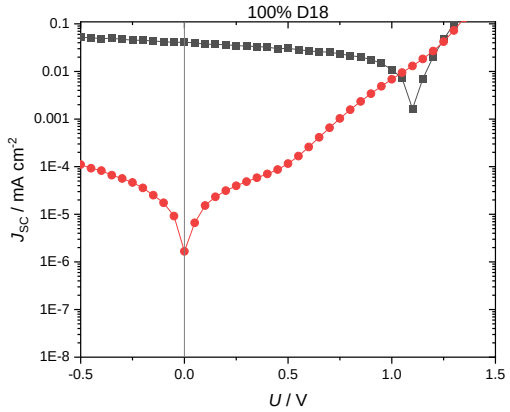

(b)

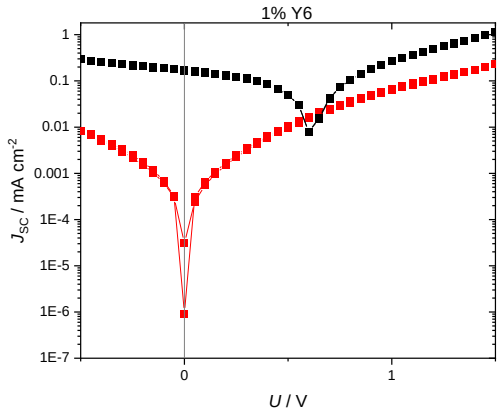

(c)

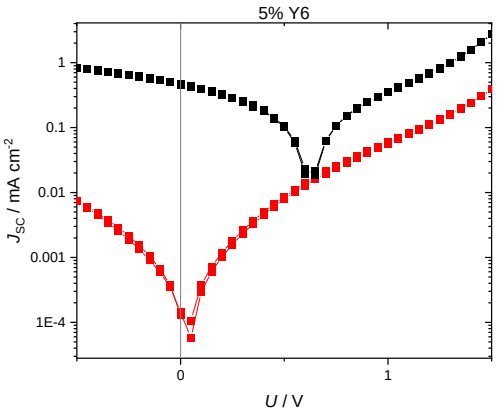

(d)

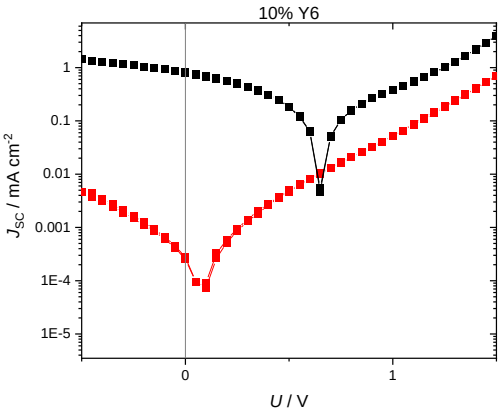

(e)

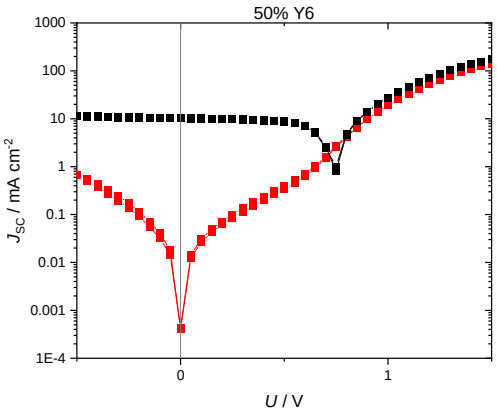

Figure 19. JV-curves of D18:Y6 OSCs with increasing acceptor concentration.

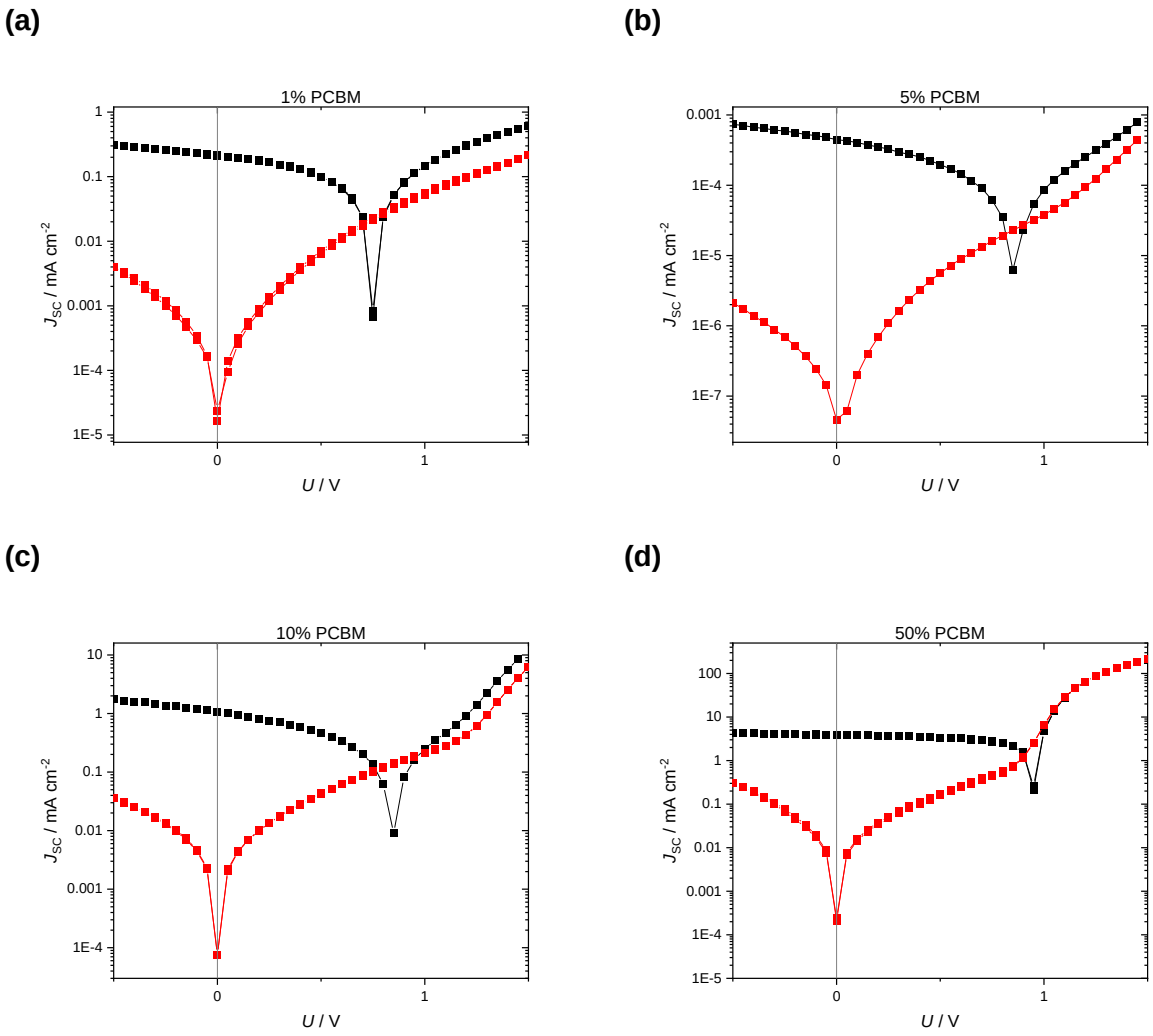

Figure 20. JV-curves of D18:$PC_{60}BM$ OSCs with increasing acceptor concentration.